RSC Advances

PAPER

View Article Online
View Journal | View Issue

Cite this: *RSC Adv.*, 2021, **11**, 26928

Constructing $NiSe_2$@MoS_2 nano-heterostructures on a carbon fiber paper for electrocatalytic oxygen evolution

Yazhou Huang, * Jiacai Huang, Kunshan Xu and Ranran Geng

Received 18th July 2021
Accepted 24th July 2021

DOI: 10.1039/d1ra05509g

rsc.li/rsc-advances

Although MoS_2 has shown its potential as an electro-catalyst for the oxygen evolution reaction (OER), its research is still insufficient. In this study, as a novel MoS_2-based heterostructure electro-catalyst for OER, namely $NiSe_2$@MoS_2 nano-heterostructure, was constructed on a carbon fiber paper (CFP) substrate by a simple approach, which includes electrochemical deposition of $NiSe_2$ film and hydrothermal processing of MoS_2 film. In addition to a series of observations on the material structure, electrocatalytic OER performance of $NiSe_2$@MoS_2 was fully evaluated and further compared with other MoS_2-based OER electro-catalysts. It exhibits an outstanding catalytic performance with an overpotential η_{10} of 267 mV and a Tafel slope of 85 mV dec^{-1}. Only 6% loss of current density before and after 10 h indicates its excellent durability. The results indicate that the obtained $NiSe_2$@MoS_2 is an excellent OER electro-catalyst and worth exploring as a substitute for noble metal-based materials.

1. Introduction

In order to solve the contradiction between environmental protection and energy demand, exploring clean energy such as hydrogen and oxygen has attracted wide attention.[1] Among different methods, splitting water into hydrogen and oxygen by the electrochemical method possesses advantages of high efficiency and abundant water resources, and is considered to be one of the most promising methods.[2–7] However, the application of this method is limited because the high overpotential in the oxygen evolution reaction (OER) process will lead to a significant loss of energy.[8] Although noble metal oxides such as IrO_2 and RuO_2 are considered to be efficient catalysts for the reduction of the OER overpotential, they cannot be used on a large scale owing to their scarcity and high-cost.[9,10] Therefore, it is of great importance to find other OER catalysts with low cost and abundant reserves, and a lot of efforts have been made in this regard.[11–18]

Recently, as a layered material, MoS_2 has been regarded as an efficient electro-catalyst for the hydrogen evolution reaction (HER) and exhibited an excellent performance.[19,20] However, research on its OER catalytic performance is still not sufficient. The theoretical calculation shows that the OER active sites of MoS_2 are at the edge with sulfur vacancies, which are similar to HER.[21] According to the reports, there are two main methods to improve the OER catalytic activity of MoS_2. The first method is to increase the exposure of the active sites by reducing the grain size and increasing the substrate gap.[22] However, the improvement is limited owing to the intrinsic structure of MoS_2.[23] The second method is to improve the electronic structure of MoS_2, for example, hybridizing MoS_2 with other materials to facilitate the chemical adsorption of oxygen-containing intermediates, so as to reduce the kinetics of OER.[24] Recently, Co/Ni-sulfide@MoS_2 heterostructures such as Co_9S_8@MoS_2,[25] CoS_2–C@MoS_2,[26] and MoS_2/Ni_3S_2 (ref. 27) have demonstrated excellent OER activities. Compared with sulfide, the electronegativity of selenide is lower, which might weaken the chemical bond between the Se atom and the bonding electrons, and thus exhibits greater activity.[28–31] For example, in the OER process, the Tafel slope of $NiSe_2$ is 97 mV dec^{-1}, which is lower than that of Ni_3S_2 (118 mV dec^{-1}).[27,32] Therefore, it is worthwhile to construct the nanoscale Ni–selenide@MoS_2 heterostructure on a substrate with abundant gaps and high conductivity as a catalyst for OER.

In this study, a novel MoS_2-based nano-heterostructure electro-catalyst, $NiSe_2$@MoS_2, was constructed on a carbon fiber paper (CFP) substrate for OER by a simple method, which includes the electrochemical deposition and hydrothermal processes. Various techniques were then employed to observe the material structure. Moreover, the electrocatalytic OER performances were fully evaluated by electrochemical measurements and further compared with other MoS_2-based OER electro-catalysts.

2. Experimental

2.1. Construction of the $NiSe_2$@MoS_2 nano-heterostructure on CFP

As shown in Fig. 1, the construction process of the $NiSe_2$@MoS_2 nano-heterostructure includes two steps: electrochemical deposition of the $NiSe_2$ film and hydrothermal synthesis of the MoS_2 film.

Industrial Center, Nanjing Institute of Technology, Nanjing 211167, People's Republic of China. E-mail: huangyazhou@njit.edu.cn

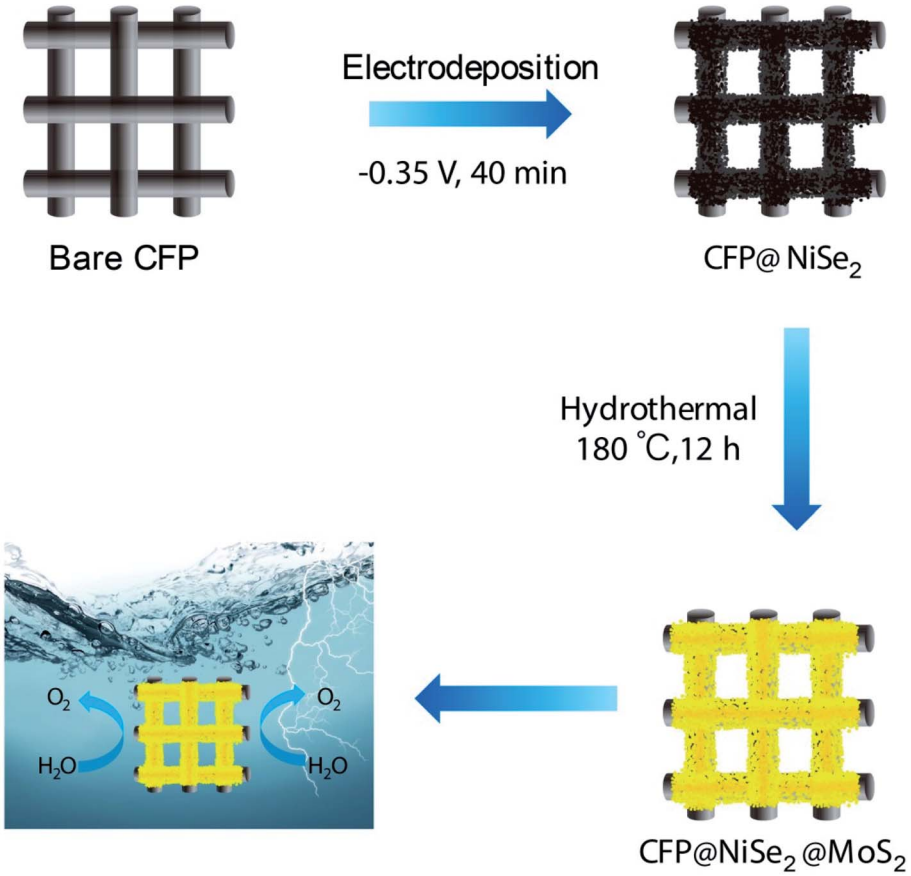

Fig. 1 Construction process of $NiSe_2$@MoS_2 nano-heterostructures on CFP.

First, the $NiSe_2$ film was electrodeposited on a carbon fiber paper (CFP, 1 × 1 cm^2, TGP-H-60, Toray) by a three-electrode electrochemical cell (CHI660E, CH Instruments). The CFP substrate, a saturated calomel electrode (SCE), and a graphite rod were employed as the working, reference, and counter electrodes, respectively. The electrolyte composed of 100 mL deionized water, 4.45 g $NiCl_2 \cdot 6H_2O$, 1.44 g SeO_2, and 1.02 g LiCl. The potential was kept at −0.35 V (*vs.* SCE) for 40 min. Then, the deposited $NiSe_2$ film (CFP@$NiSe_2$) was washed using deionized water and dried in a vacuum drying oven at 60 °C.

Second, the MoS_2 film was coated on CFP@$NiSe_2$ by the hydrothermal synthesis. In this process, the amount of precursor and technological conditions are very strict. The precursor solution, including 0.06 g $(NH_4)_6Mo_7O_{24} \cdot 4H_2O$, 0.15 g $SC(NH_2)_2$, and 30 mL deionized water, was magnetically stirred for 5 min and allowed to stand at 60 °C for 1 h. Then, it was transferred into a 50 mL airtight reactor and was allowed to stand at 180 °C for 12 h to afford CFP@$NiSe_2$@MoS_2. It was washed with deionized water and dried in a vacuum drying oven at 60 °C. Detailed procedures refer to ref. 33.

2.2. Characterization

First, the material structure of the obtained samples was observed by various means. The morphology observation was carried out *via* scanning electron microscopy (SEM, S-4800, Hitachi), high-resolution transmission electron microscopy (HRTEM, TECNAI G2F20, FEI), and X-ray diffraction (XRD, X'Pert3, Panalytical). Before TEM characterization, the samples were ground into powder and transferred to a copper grid. XRD was carried out with Cu Kα radiation ($\lambda = 1.54$ Å) at 40 mA and 45 kV. The chemical elements of samples were observed *via* energy dispersive spectroscopy (EDS, S-4800, Hitachi) and X-ray photoelectron spectroscopy (XPS, EscaLab-250Xi, Thermofisher). XPS source is Al Kα ($h\nu = 1486.6$ eV) with a power of 22.8 W.

Second, the electrocatalytic OER performances of the obtained samples were observed through a three-electrode electrochemical cell that employs Hg/HgO and graphite rod as reference and counter electrodes, respectively, in a 1 M KOH electrolyte solution. Before the measurement, high-purity oxygen was injected into the electrolyte for 20 min to eliminate the interference of oxygen. Then, the oxygen bubbles formed on the electrode surface were dislodged by magnetic stirring during the process of measurement. The potential E_{RHE} was obtained by the equation of $E_{RHE} = E_{Hg/HgO} + 0.059pH + 0.098$. OER polarization curves were obtained by linear sweep voltammetry (LSV) at a scan rate of 10 mV s^{-1} from 0.5 to 2 V (*vs.* RHE). The result was corrected by the equation of $\eta_{corr} = \eta_{exp} - iR$ to eliminate the effect of series resistance. Electrochemical impedance spectra (EIS) were obtained at 1.51 V (*vs.* RHE) in

a frequency range of 10^5–0.1 Hz with an amplitude of 5 mV. The double-layer capacitance (C_{dl}), obtained by cyclic voltammetry (CV) tests at different scan rates from 20 to 200 mV s^{-1} in a range of 0.68–0.78 V (*vs.* RHE), was used to evaluate the electrochemically active surface area (ECSA).

3. Results and discussion

$NiSe_2$ and MoS_2 films were coated on a CFP substrate, respectively. According to Fig. 2(a–c), rich voids between carbon fibers in the CFP substrate can enlarge the contact of the catalyst to the electrolyte, which are beneficial to improving the OER activity. According to the enlarged view in the inset, due to the poor crystallinity induced by the low temperature in the constructing process, both $NiSe_2$ and MoS_2 nanosheets are disorderly distributed in the film. Owing to the disorderly distribution, abundant edges of $NiSe_2$ and MoS_2 nanosheets can further improve the contact area and activity. Moreover, the close contact between $NiSe_2$ and CFP obtained by the electrochemical deposition can reduce the charge transfer impedance in the OER process. As shown in Fig. 2(d), the thickness of the $NiSe_2$@MoS_2 film is ~550 nm. According to further HRTEM observation (Fig. 2(e)), the $NiSe_2$@MoS_2 heterostructure is composed of 0.27 nm MoS_2 (002) face and 0.66 nm $NiSe_2$ (210)

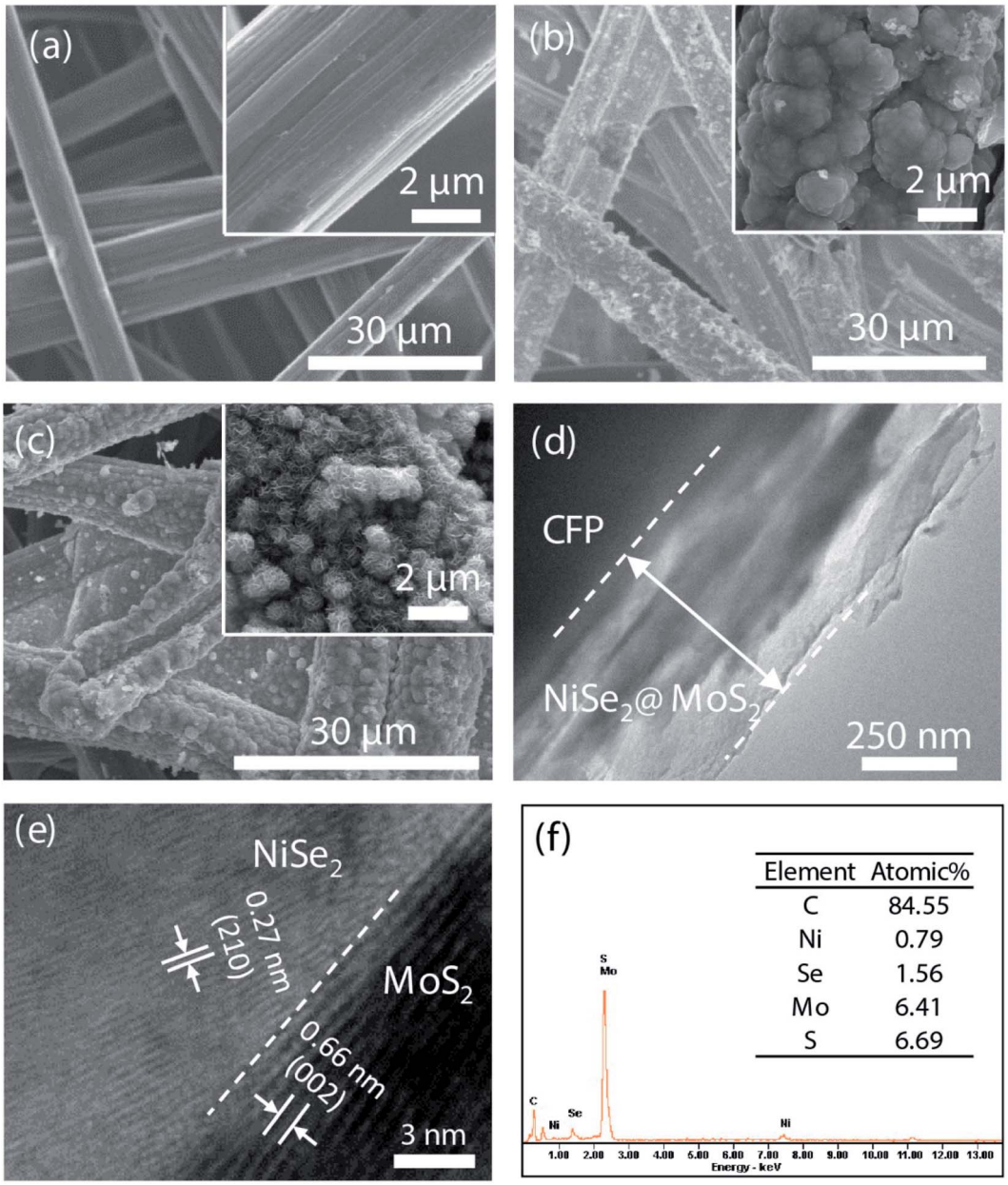

Fig. 2 SEM images of (a) CFP, (b) CFP@$NiSe_2$, (c) CFP@$NiSe_2$@MoS_2. (d) TEM result of CFP@$NiSe_2$@MoS_2. (e) HRTEM result of $NiSe_2$@MoS_2. The $NiSe_2$@MoS_2 nano-heterostructure composed of MoS_2 (002) and $NiSe_2$ (210) faces can be clearly observed. (f) EDS results of CFP@$NiSe_2$@MoS_2. Ratio of Se/Ni is close to 2, while that of S/Mo is close to 1, indicating that it is sulfur deficient.

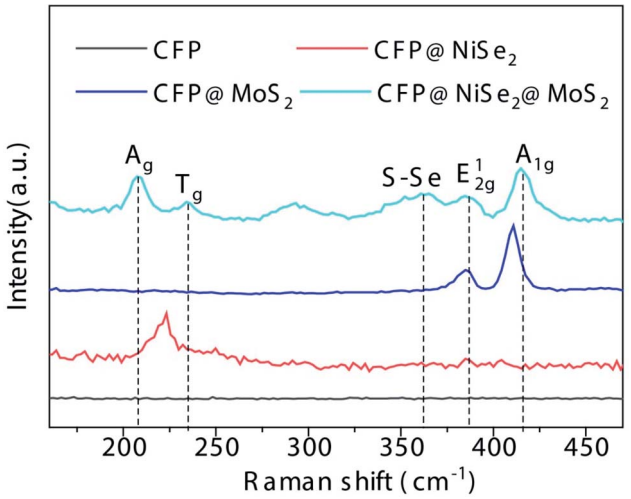

Fig. 3 Raman results of the samples. Peaks A_g and T_g belong to $NiSe_2$, while E^1_{2g} and A_{1g} belong to MoS_2. The presence of the peak S–Se confirms that the $NiSe_2$@MoS_2 heterostructure was formed.

face. EDS spectra were further recorded to observe the element composition of the heterostructure (Fig. 2(f)). The ratio of Se/Ni is close to 2 while that of S/Mo is close to 1, indicating that the obtained $NiSe_2$@MoS_2 is sulfur deficient.

As shown in Fig. 3, the samples were further observed by Raman spectroscopy. In the spectrum of CFP@$NiSe_2$@MoS_2, peaks A_g and T_g of $NiSe_2$ are shown at ~208 and ~235 cm^{-1}, respectively, while E^1_{2g} and A_{1g} of MoS_2 are shown at ~379 and ~405 cm^{-1}, respectively, indicating that $NiSe_2$@MoS_2 is indeed deposited on CFP.[34,35] The interfering peak at ~290 cm^{-1}, originating from internal strain of MoS_2, is caused by the disorder of the grains and defects.[36] The S–Se peak at ~360 cm^{-1}, originating from S–Se pairs, further confirms that the $NiSe_2$@MoS_2 heterostructure is formed.[37] Compared with CFP@MoS_2, peaks E^1_{2g} and A_{1g} of MoS_2 in CFP@$NiSe_2$@MoS_2 exhibit an obvious blue shift, because the crystal symmetry is destroyed by the defects. The defects are from the $NiSe_2$ substrate and $NiSe_2$@MoS_2 heterostructures, which can improve the exposure of active sites and OER activity of MoS_2.[38–40] Moreover, peaks A_g and T_g cannot be observed independently in CFP@$NiSe_2$, indicating that the crystallinity of $NiSe_2$ prepared by the electrochemical deposition is relatively low. Then, the crystallinity is improved by the subsequent hydrothermal process of MoS_2, which helps to reduce the charge transfer impedance in the process of OER.

As shown in Fig. 4, structures of the samples were also observed by XRD. The standard diffraction peaks of $NiSe_2$ and MoS_2 are shown in PDF no. 41-1945 and no. 37-1942, respectively. Peaks at 26.3 and 54.2° originate from the CFP substrate. In the spectra of CFP@$NiSe_2$, peaks corresponding to (200), (210), (211), (220), (311), and (321) planes of $NiSe_2$ are clearly shown at around 29.4, 33.5, 36.6, 43.5, 50.7, and 57.5°, respectively.[32] According to the spectra of CFP@MoS_2, the (002) peak of MoS_2 can be observed at 13.1°. The simultaneous appearance of peaks of $NiSe_2$ and MoS_2 in CFP@$NiSe_2$@MoS_2 further confirms that $NiSe_2$ and MoS_2 are successfully deposited on the

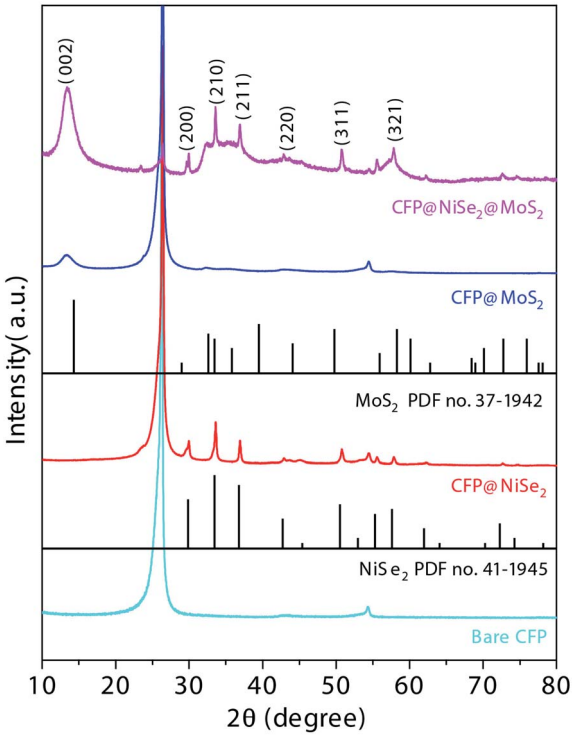

Fig. 4 XRD spectra of the samples. The standard diffraction peaks of $NiSe_2$ and MoS_2 are shown in PDF no. 41-1945 and no. 37-1942 respectively. Peaks (002) of MoS_2, (200), (210), (211), (220), (311), and (321) of $NiSe_2$ are clearly exhibited.

CFP substrate. Moreover, compared with CFP @MoS_2, the (002) peak has a blue shift from 13.1 to 13.5 in CFP@$NiSe_2$@MoS_2 owing to the defects from the $NiSe_2$ substrate and $NiSe_2$@MoS_2 heterostructures. This structure is in favor of the improvement of the OER activity, which is consistent with the Raman results.

The composition of the samples was further analyzed by XPS. According to the spectra of Ni 2p and Se 3d shown in Fig. 5(a and b), peaks of Ni $2p_{1/2}$ and Ni $2p_{3/2}$ belonging to Ni^{4+} of $NiSe_2$ are shown at 870.2 and 853.1 eV with their satellite peaks at 875.7 and 859.2 eV, respectively.[41] Peaks of Se $3d_{3/2}$ and Se $3d_{5/2}$ at 53.5 and 52.7 eV, respectively, belong to Se_2^{2-} of $NiSe_2$, while an oxidized Se peak is shown at 57 eV.[42] Moreover, as shown in Fig. 5(c and d), peaks of Mo $3d_{3/2}$ and Mo $3d_{5/2}$ at 231.2 and 228 eV are attributed to Mo^{4+} of MoS_2, and the peak at 225.5 eV is due to the Mo–S bond. Peaks of S $2p_{1/2}$ and S $2p_{3/2}$ at 161.8 and 160.8 eV are due to S_2^{2-} of MoS_2.[43] Therefore, $NiSe_2$ and MoS_2 have been deposited on CFP successfully. In addition, compared with CFP@$NiSe_2$ and CFP@MoS_2, peaks of Ni 2p and Se 3d show a negative shift, while those of Mo 3d and S 2p have a positive shift in CFP@$NiSe_2$@MoS_2, further confirming that the $NiSe_2$@MoS_2 heterostructure has been formed.[44] The Mo-to-S ratio also needs to be observed because OER active sites of MoS_2 have been shown at its edge with S-vacancies.[21] According to the peaks of Mo 3d and S 2p shown in Fig. 5(c and d), compared with CFP@MoS_2, the Mo/S ratio increases from 0.81 to 0.93 in CFP@$NiSe_2$@MoS_2, indicating that S-vacancies increase by about 15% in the latter. Thus, the obtained $NiSe_2$@MoS_2 can expose more active sites and improve the OER activity.

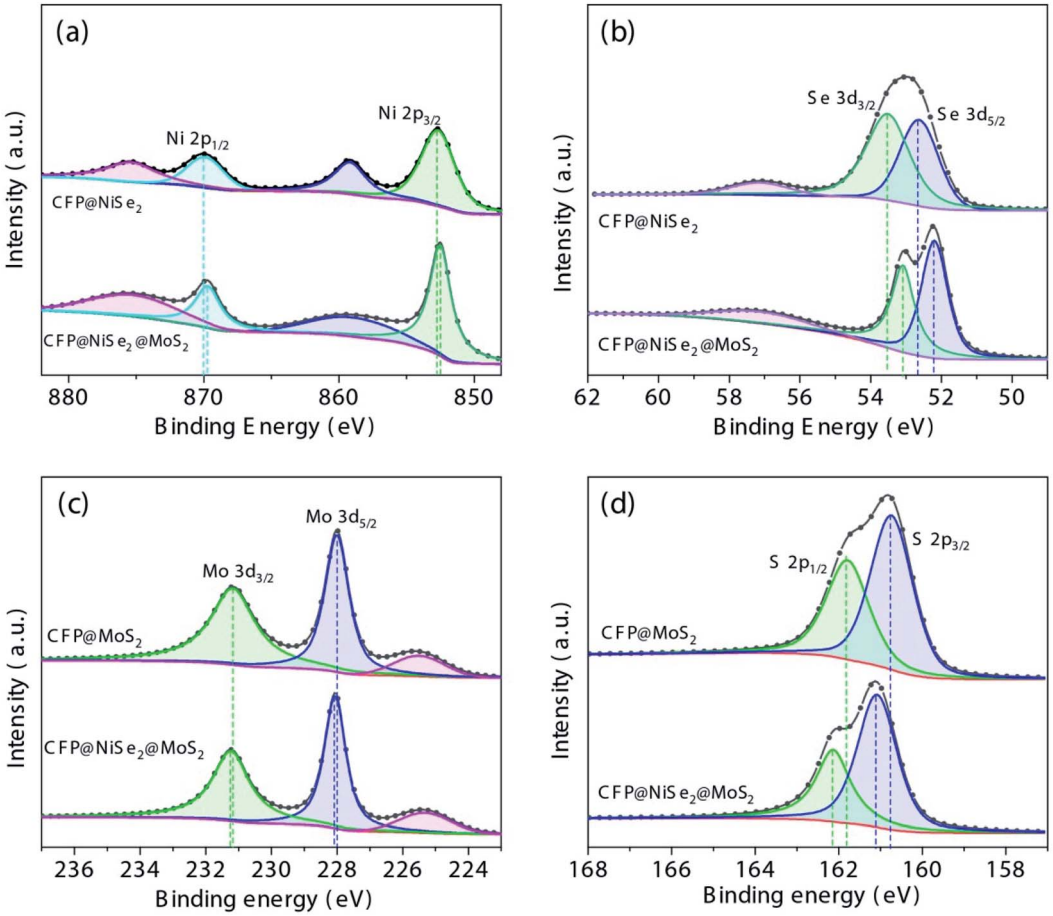

Fig. 5 XPS spectra of (a) Ni 2p, (b) Se 3d, (c) Mo 3d, and (d) S 2p.

The electrocatalytic OER performances of the samples were evaluated by various electrochemical measurements. The OER polarization curves obtained by LSV in 1 M KOH solution are shown in Fig. 6(a). Unsurprisingly, the bare CFP with an almost zero current density shows no electrocatalytic OER activity in the potential window from 1.2 to 1.7 V (*vs.* RHE). For CFP@MoS_2, the potential driving the current density of 10 mA cm^{-2} needs 1.62 V (*vs.* RHE), which indicates an overpotential η_{10} of 390 mV. Although it has some reduction than CFP, it is still relatively high and worthless as an OER catalyst. In the curve of CFP@$NiSe_2$, the peak at ~1.36 V (*vs.* RHE) is attributed to the oxidation of Ni.[32,45] It was first oxidized to $Ni(OH)_2$, which proceeded as $Ni + 2OH^- \rightarrow Ni(OH)_2 + 2e^-$. As the potential increased, $Ni(OH)_2$ was further oxidized to NiOOH, which proceeded as $Ni(OH)_2 + OH^- \rightarrow NiOOH + H_2O + e^-$. The overpotential η_{10} of 290 mV is lower than that of CFP@MoS_2. When the current density increases to 20 mA cm^{-2}, the overpotential η_{20} of 356 mV is also lower than that of CFP@MoS_2 (440 mV), indicating a better activity. However, it is not the best. Obviously, CFP@$NiSe_2$@MoS_2 with η_{10} of 267 mV and η_{20} of 320 mV exhibits the highest catalytic performance.

Tafel slopes of the samples were further observed by fitting the polarization curves with the Tafel equation ($\eta = a + b \log j$, where b is the Tafel slope). According to Fig. 6(b) and Table 1, Tafel slopes of the samples are 159, 112, and 85 mV dec^{-1}, respectively. The much smaller Tafel slope of CFP@$NiSe_2$@MoS_2 further confirms its excellent OER catalytic performance. It is also compared with that of other MoS_2-based and noble metal oxide electro-catalysts reported recently (Table 2). CFP@MoS_2 with η_{10} of 390 mV and b of 159 mV dec^{-1} shows an obvious activity improvement than the exfoliated MoS_2, which can be attributed to the more exposure of active sites induced by the small grain.[23] Compared with CFP@MoS_2, the performance of CFP@$NiSe_2$@MoS_2 has a further improvement. Moreover, the performance of CFP@$NiSe_2$@MoS_2 and MoS_2/Ni_3S_2 is similar. However, compared to the dependence of MoS_2/Ni_3S_2 on nickel foam, $NiSe_2$@MoS_2 can be deposited on the surface of any conductor as shown in this study, which greatly expands its application.[27] Compared with that of Co_3S_4@MoS_2, CoS_2–C@MoS_2, Co_3O_4@MoS_2/CC, and RuO_2, although the Tafel slope of CFP@$NiSe_2$@MoS_2 is bigger, it has a smaller overpotential η_{10}, indicating that CFP@$NiSe_2$@MoS_2 is an excellent OER electro-catalyst and worth exploring as a substitute for noble metal-based materials.

As shown in Fig. 6(c), electrochemical impedance spectra (EIS) of the samples were measured and fitted by the equivalent circuit (Fig. 6(d)), where R_s is the series resistance, R_{ct} is the charge-transfer resistance, and CPE is the constant phase

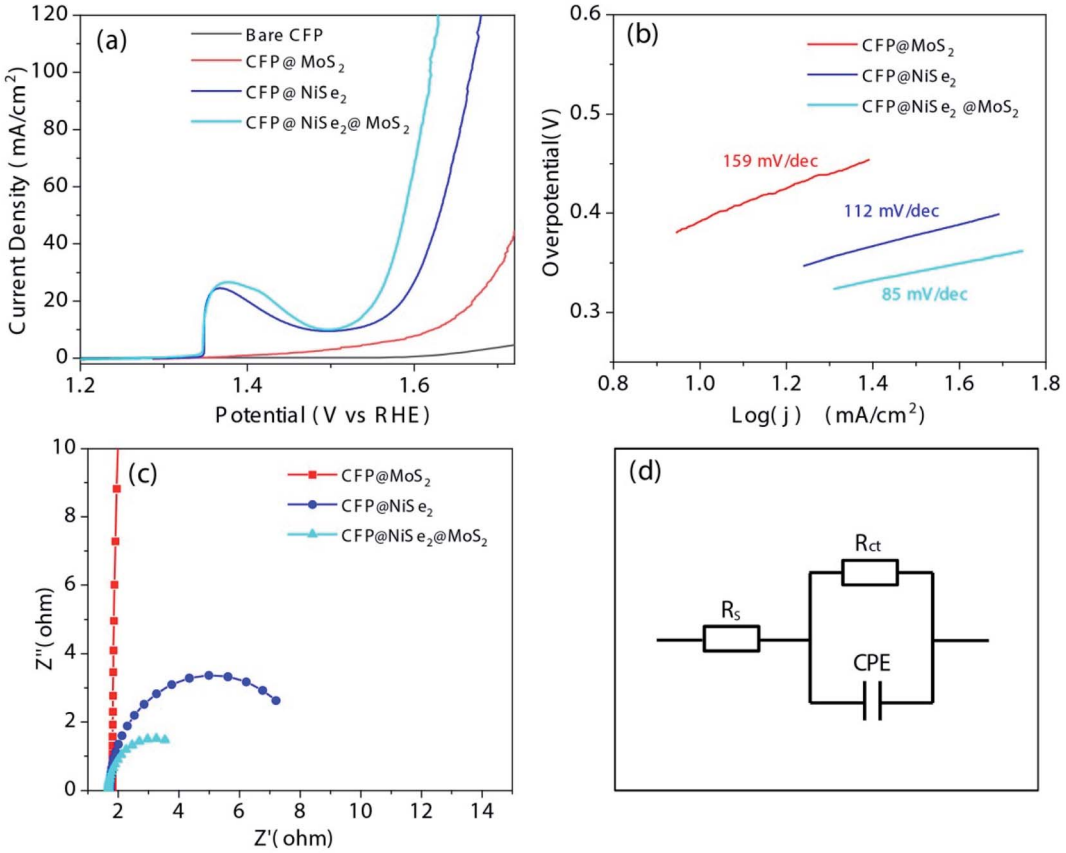

Fig. 6 (a) OER polarization curves, (b) Tafel plots, and (c) impedance analysis of the samples. (d) The equivalent circuit: R_s is the series resistance, R_{ct} is the charge-transfer resistance, and CPE is the constant phase elements.

elements. According to Fig. 6(c) and Table 3, R_s and R_{ct} of the samples are 1.81 and 567.6, 1.71 and 6.74, 1.68 and 3.03 Ω, respectively. It can be obtained that R_s values of the samples are slightly different. However, the R_{ct} value has a significant decrease from 567.6 to 3.03 Ω, which indicates that CFP@$NiSe_2$@MoS_2 can substantially improve the OER activity.

C_{dl} was used to evaluate ECSA of the samples. As shown in Fig. 7(a–c), CV tests of the samples were performed with different scan rates from 20 to 200 mV s^{-1} in the regions of non-faradaic potentials (0.68–0.78 V (*vs.* RHE)). Current density differences between anodic and cathodic *versus* the scanning rate at 0.73 V a (*vs.* RHE) are shown in Fig. 7(d). Fitting these data linearly can obtain the C_{dl} value. According to Fig. 7(d) and Table 3, C_{dl} values of the samples are 0.78, 4.64, and 6.25 mF cm^{-2}, respectively. The much larger C_{dl} of CFP@$NiSe_2$@MoS_2 among the samples indicates that the ECSA was significantly increased. Hence, the outstanding OER performance of CFP@$NiSe_2$@MoS_2 is not only due to the faster electron transfer rate but also due to the increasing ECSA.

Table 1 Overpotential and Tafel slope of the obtained samples

Catalyst	Overpotential η_{10} (mV)	Overpotential η_{20} (mV)	Tafel slope b (mV dec^{-1})
CFP@$NiSe_2$@MoS_2	267	320	85
CFP@$NiSe_2$	290	356	112
CFP@MoS_2	390	440	159

Table 2 The electrocatalytic OER performances of CFP@$NiSe_2$@MoS_2 and other MoS_2-based electro-catalysts

Catalyst	Tafel slope b (mV dec^{-1})	Overpotential η_{10} (mV)	Ref.
CFP@$NiSe_2$@MoS_2	85	267	This work
CFP@MoS_2	159	390	This work
Exfoliated MoS_2	322	420	46
Co_9S_8@MoS_2	94	342	25
Co_3S_4@MoS_2	43	280	47
CoS_2–C@MoS_2	46	391	26
MoS_2/Ni_3S_2	88	218	27
Co_3O_4@MoS_2/CC	58	360	48
RuO_2	65	380	49

Table 3 Series resistance R_s, charge-transfer resistance R_{ct}, and double-layer capacitance C_{dl} of the obtained samples

Catalyst	Resistance R_s (Ω)	Resistance R_{ct} (Ω)	C_{dl} (mF cm^{-2})
CFP@$NiSe_2$@MoS_2	1.68	3.03	0.78
CFP@$NiSe_2$	1.71	6.74	4.64
CFP@ MoS_2	1.81	567.6	6.25

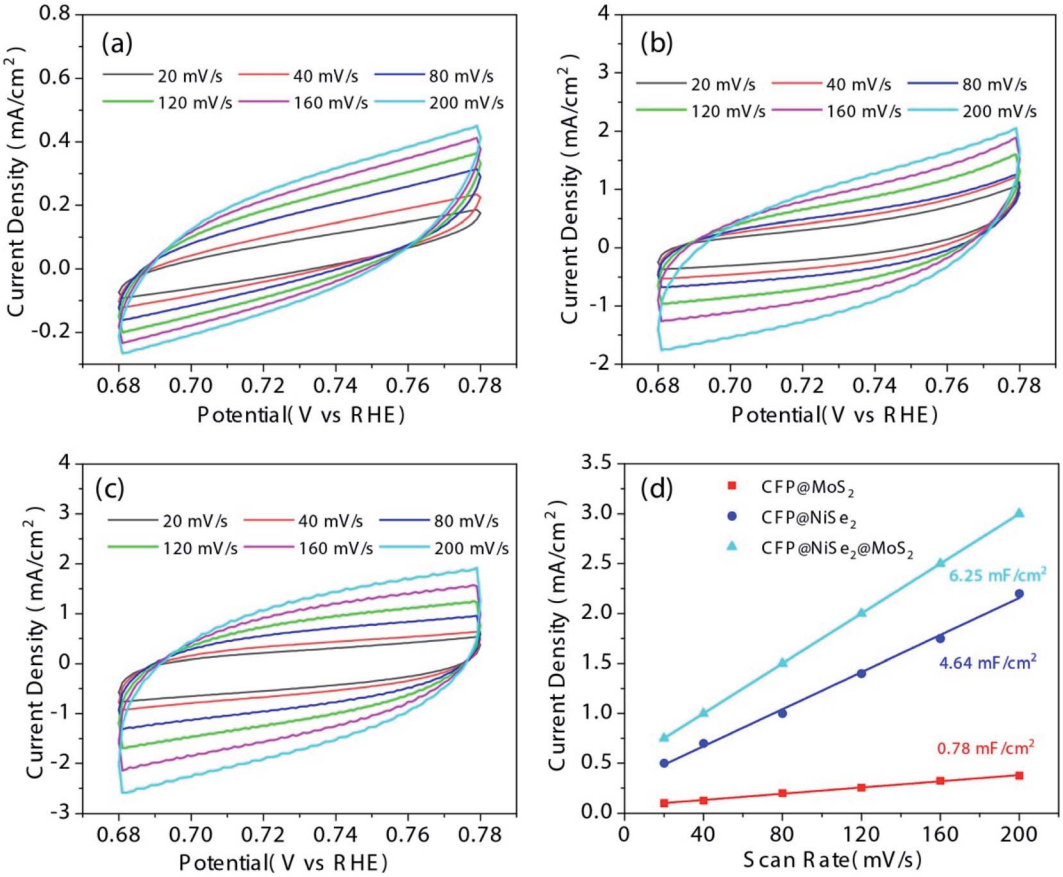

Fig. 7 CV tests of (a) CFP@MoS_2, (b) CFP@$NiSe_2$, and (c) CFP@$NiSe_2$@MoS_2 with different scan rates from 20 to 200 mV s^{-1} in a range of 0.68–0.78 V (*vs.* RHE). (d) Current density difference between anodic and cathodic *versus* the scanning rate at 0.73 V a (*vs.* RHE). C_{dl} obtained by linear fitting the data was used to evaluate ECSA of the samples because C_{dl} was proportional to ECSA.

The durability of CFP@$NiSe_2$@MoS_2 was further measured by repeating the CV test for 1000 cycles. According to Fig. 8(a), the difference in current density is negligible before and after 1000 cycles. The current density *versus* time under a constant overpotential of 340 mV is shown in Fig. 8(b). Only 6% loss after 10 h indicates its outstanding durability.

The mechanism that $NiSe_2$@MoS_2 has a better catalytic performance than pure MoS_2 or $NiSe_2$ can be summarized as follows:

(1) The disordered $NiSe_2$ increases the contact area between MoS_2 and the electrolyte solution. $NiSe_2$@MoS_2 samples are obtained by depositing MoS_2 on $NiSe_2$, while pure MoS_2 and $NiSe_2$ are deposited directly on the bare CFP substrate. Compared with the smooth bare CFP substrate, the disordered distribution of $NiSe_2$ nanosheets (as shown in Fig. 2) can further increase the superficial area of MoS_2, so as to increase the contact area between MoS_2 and the electrolyte solution. This is an effective way to improve the OER efficiency of MoS_2.

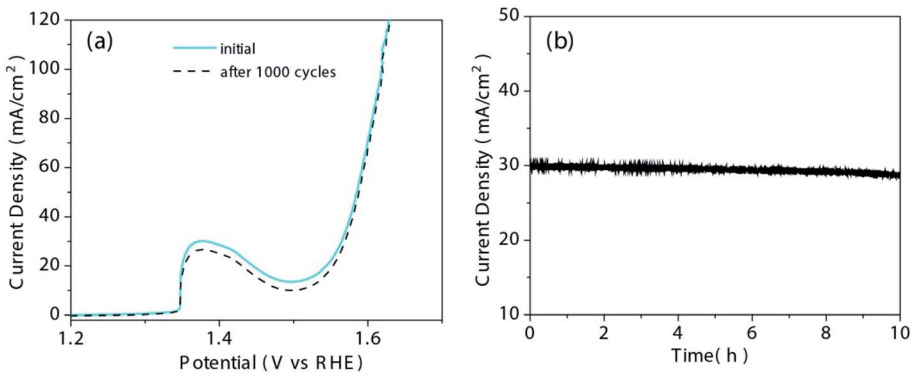

Fig. 8 (a) Durability measurement of CFP@$NiSe_2$@MoS_2. Difference in current density is negligible before and after 1000 cycles. (b) The current density *versus* time under a constant overpotential of 340 mV.

According to the C_{dl} results (as shown in Fig. 7), the ECSA of $NiSe_2$@MoS_2 significantly increased than that of pure $NiSe_2$ and MoS_2.

(2) The hybridization of $NiSe_2$ increases the defects of MoS_2, which can improve the exposure of active sites and OER activity of MoS_2. It has been demonstrated that defects such as doping, atomic vacancy and lattice distortion can increase the exposure of active sites of MoS_2.[38–40] According to the results of the material characterization, the defects of MoS_2 do increase in $NiSe_2$@MoS_2. As shown in the Raman results (Fig. 3), some phenomena in $NiSe_2$@MoS_2 such as the appearance of the interfering peak at ~290 cm^{-1}, the blue shift and expansion of the characteristic peak of MoS_2, indicate that the crystal symmetry of MoS_2 was damaged by the defects.

According to the XPS results (Fig. 5), the ~15% increase of S-vacancies in $NiSe_2$@MoS_2 confirms that the hybridization of $NiSe_2$ increases the exposure of active sites of MoS_2.

(3) Doping Ni atoms into MoS_2 at the interface of the $NiSe_2$@MoS_2 heterostructure can effectively reduce the kinetic energy barrier of the initial water-dissociation step and facilitate the desorption of –OH,[27] so as to improve the OER performance. According to Raman and XPS results (Fig. 3 and 5), it can be confirmed that the chemical bonds between $NiSe_2$ and MoS_2 are generated at the interface of the $NiSe_2$@MoS_2 heterostructure.

4. Conclusion

In summary, the novel $NiSe_2$@MoS_2 nano-heterostructure for electrocatalytic OER has been constructed on a CFP substrate by a simple method. The electrocatalytic OER performances were fully evaluated by electrochemical measurements and further compared with that of other MoS_2-based and noble metal oxide electro-catalysts. It exhibits an outstanding catalytic performance with an overpotential η_{20} of 323 mV and a Tafel slope of 85 mV dec^{-1}. Just 6% loss of current density before and after 10 h also indicates its excellent durability. Therefore, it is an excellent OER electro-catalyst and worth exploring as a substitute for noble metal-based materials.

Author contributions

Yazhou Huang: resources, conceptualization, methodology, investigation, writing – original draft, writing – review & editing. Jiacai Huang: writing – review & editing, methodology, formal analysis. Kunshan Xu: methodology, data curation. Ranran Geng: validation, formal analysis.

Conflicts of interest

There are no conflicts to declare.

Acknowledgements

This work was supported by the National Natural Science Foundation of China (51905259), the Natural Science Foundation of Jiangsu Province (BK20191017), the Natural Science Research Program for Higher Education of Jiangsu Province (19KJB460003, 20KJA510007), the Scientific Research Fund of Nanjing Institute of Technology (YKJ201859).

References

1 M. S. Dresselhaus and I. L. Thomas, *Nature*, 2001, **414**, 332–337.
2 A. Yamaguchi, R. Inuzuka, T. Takashima, T. Hayashi, K. Hashimoto and R. Nakamura, *Nat. Commun.*, 2014, **5**, 4256.
3 L. Gao, X. Cui, Z. Wang, C. D. Sewell, Z. Li, S. Liang, M. Zhang, J. Li, Y. Hu and Z. Lin, *Proc. Natl. Acad. Sci. U. S. A.*, 2021, **118**, e2023421118.
4 G. Liao, J. Fang, Q. Li, S. Li, Z. Xu and B. Fang, *Nanoscale*, 2019, **11**, 7062–7096.
5 Y. Zhang, X. Wang, F. Luo, Y. Tan, L. Zeng, B. Fang and A. Liu, *Appl. Catal., B*, 2019, **256**, 117852.
6 S. Shen, Z. Lin, K. Song, Z. Wang, L. Huang, L. Yan, F. Meng, Q. Zhang, L. Gu and W. Zhong, *Angew. Chem., Int. Ed.*, 2021, **60**, 12360–12365.
7 Z. Lin, S. Shen, Z. Wang and W. Zhong, *iScience*, 2021, **24**, 102469.
8 C. C. Mccrory, S. Jung, J. C. Peters and T. F. Jaramillo, *J. Am. Chem. Soc.*, 2013, **135**, 16977–19687.
9 J. Wang, W. Cui, Q. Liu, Z. Xing, A. M. Asiri and X. Sun, *Adv. Mater.*, 2016, **28**, 215–230.
10 W. Zhong, Z. Lin, S. Feng, D. Wang, S. Shen, Q. Zhang, L. Gu, Z. Wang and B. Fang, *Nanoscale*, 2019, **11**, 4407–4413.
11 L. Xu, Z. Wang, J. Wang, Z. Xiao, X. Huang, Z. Liu and S. Wang, *Nanotechnology*, 2017, **28**, 165402.
12 H. Li, Y. Shao, Y. Su, Y. Gao and X. Wang, *Chem. Mater.*, 2016, **28**, 1155–1164.
13 J. R. Swierk, S. Klaus, L. Trotochaud, A. T. Bell and T. D. Tilley, *J. Phys. Chem. C*, 2015, **119**, 19022–19029.
14 T. Chun, C. Ningyan, P. Zonghua, X. Wei and S. Xuping, *Angew. Chem., Int. Ed.*, 2015, **54**, 9351–9355.
15 L. Feng, F. Song and X. Hu, *Energy Environ. Sci.*, 2015, **8**, 2347–2351.
16 X. Cui, S. Lei, A. C. Wang, L. Gao, Q. Zhang, Y. Yang and Z. Lin, *Nano Energy*, 2020, **70**, 104525.
17 A. Xu, W. Tu, S. Shen, Z. Lin, N. Gao and W. Zhong, *Appl. Surf. Sci.*, 2020, **528**, 146949.
18 Z. Wang, Z. Lin, J. Deng, S. Shen, F. Meng, J. Zhang, Q. Zhang, W. Zhong and L. Gu, *Adv. Energy Mater.*, 2021, **11**, 2003023.
19 Y. Yan, B. Y. Xia, Z. Xu and X. Wang, *ACS Catal.*, 2014, **4**, 1693–1705.
20 J. D. Benck, Z. B. Chen, L. Y. Kuritzky, A. J. Forman and T. F. Jaramillo, *ACS Catal.*, 2012, **2**, 1916–1923.
21 B. Mohanty, M. Ghorbani-Asl, S. Kretschmer, A. Ghosh, P. Guha, S. K. Panda, B. Jena, A. V. Krasheninnikov and B. K. Jena, *ACS Catal.*, 2018, **8**, 1683–1689.
22 D. Xiong, Q. Zhang, W. Li, J. Li, X. Fu, M. F. Cerqueira, P. Alpuim and L. Liu, *Nanoscale*, 2017, **9**, 2711–2717.
23 Y. Huang, L. Liu and X. Liu, *Nanotechnology*, 2019, **30**, 095402.

24 H. Zhu, J. Zhang, R. Yanzhang, M. Du, Q. Wang, G. Gao, J. Wu, G. Wu, M. Zhang, B. Liu, J. Yao and X. Zhang, *Adv. Mater.*, 2015, **27**, 4752–4759.
25 J. Bai, T. Meng, D. Guo, S. Wang, B. Mao and M. Cao, *ACS Appl. Mater. Interfaces*, 2018, **10**, 1678–1689.
26 Y. Zhu, L. Song, N. Song, M. Li, C. Wang and X. Lu, *ACS Sustainable Chem. Eng.*, 2019, **7**, 2899–2905.
27 J. Zhang, T. Wang, D. Pohl, B. Rellinghaus, R. Dong, S. Liu, X. Zhuang and X. Feng, *Angew. Chem.*, 2016, **128**, 6814–6819.
28 X. Zhao, Y. Yang, Y. Li, X. Cui, Y. Zhang and P. Xiao, *J. Mater. Sci.*, 2016, **51**, 3724–3734.
29 W. Zhong, Z. Wang, N. Gao, L. Huang, Z. Lin, Y. Liu, F. Meng, J. Deng, S. Jin, Q. Zhang and L. Gu, *Angew. Chem., Int. Ed.*, 2020, **59**, 22743–22748.
30 W. Zhong, B. Xiao, Z. Lin, Z. Wang, L. Huang, S. Shen, Q. Zhang and L. Gu, *Adv. Mater.*, 2021, **33**, 2007894.
31 Z. Lin, B. Xiao, Z. Wang, W. Tao, S. Shen, L. Huang, J. Zhang, F. Meng, Q. Zhang, L. Gu and W. Zhong, *Adv. Funct. Mater.*, 2021, 2102321.
32 J. Zhu and Y. Ni, *CrystEngComm*, 2018, **20**, 3344–3352.
33 Y. Huang, J. Lv, J. Huang, K. Xu and L. Liu, *Nanotechnology*, 2021, **32**, 175602.
34 F. Wang, Y. Li, T. A. Shifa, K. Liu, F. Wang, Z. Wang, P. Xu, Q. Wang and J. He, *Angew. Chem., Int. Ed.*, 2016, **55**, 6919–6924.
35 L. Liu, Y. Huang, J. Sha and Y. Chen, *Nanotechnology*, 2017, **28**, 195605.
36 Z. Jin, S. Shin, D. H. Kwon, S.-J. Han and Y.-S. Min, *Nanoscale*, 2014, **6**, 14453–14458.
37 C. d. l. Heras and F. Agulló-Rueda, *J. Phys.: Condens. Matter*, 2000, **12**, 5317–5324.
38 J. Xie, H. Zhang, S. Li, R. Wang, X. Sun, M. Zhou, J. Zhou, X. W. Lou and Y. Xie, *Adv. Mater.*, 2013, **25**, 5807–5813.
39 H. Li, C. Tsai, A. L. Koh, L. Cai, A. W. Contryman, A. H. Fragapane, J. Zhao, H. S. Han, H. C. Manoharan, F. Abild-Pedersen, J. K. Nørskov and X. Zheng, *Nat. Mater.*, 2016, **15**, 48–53.
40 J. Zhang, X. Xu, L. Yang, D. Cheng and D. Cao, *Small Methods*, 2019, **3**, 1900653.
41 I. H. Kwak, H. S. Im, D. M. Jang, Y. W. Kim, K. Park, Y. R. Lim, E. H. Cha and J. Park, *ACS Appl. Mater. Interfaces*, 2016, **8**, 5327–5334.
42 J. Liang, Y. Yang, J. Zhang, J. Wu, P. Dong, J. Yuan, G. Zhang and J. Lou, *Nanoscale*, 2015, **7**, 14813–14816.
43 L. Liu, X. Liu and S. Jiao, *J. Colloid Interface Sci.*, 2020, **564**, 77–87.
44 S. Li, W. Zang, X. Liu, S. J. Pennycook, Z. Kou, C. Yang, C. Guan and J. Wang, *Chem. Eng. J.*, 2019, **359**, 1419–1426.
45 M. W. Louie and A. T. Bell, *J. Am. Chem. Soc.*, 2013, **135**, 12329–12337.
46 J. Wu, M. Liu, K. Chatterjee, K. P. Hackenberg, J. Shen, X. Zou, Y. Yan, J. Gu, Y. Yang, J. Lou and P. M. Ajayan, *Adv. Mater. Interfaces*, 2016, **3**, 1500669.
47 Y. Guo, J. Tang, Z. Wang, Y.-M. Kang, Y. Bando and Y. Yamauchi, *Nano Energy*, 2018, **47**, 494–502.
48 J. Liu, J. Wang, B. Zhang, Y. Ruan, H. Wan, X. Ji, K. Xu, D. Zha, L. Miao and J. Jiang, *J. Mater. Chem. A*, 2018, **6**, 2067–2072.
49 S. Jung, C. C. L. McCrory, I. M. Ferrer, J. C. Peters and T. F. Jaramillo, *J. Mater. Chem. A*, 2016, **4**, 3068–3076.